Applied Surface Science 564 (2021) 150474

Contents lists available at ScienceDirect

Applied Surface Science

journal homepage: www.elsevier.com/locate/apsusc

Full Length Article

AuPt Nanoparticles/ Multi-Walled carbon nanotubes catalyst as high active and stable oxygen reduction catalyst for Al-Air batteries

Zhihong Luo [a], Liankun Yin [a], Li Xiang [a], Terence Xiaoteng Liu [c,*], Zhou Song [d], Yibing Li [a], Li Zhou [a], Kun Luo [b,*], Kai Wu [e], Jianjie Jiang [e]

[a] Guangxi Key Laboratory of Optical and Electronic Materials and Devices, School of Materials Science and Engineering, Guilin University of Technology, Guilin 541004, China
[b] School of Materials Science and Engineering, Changzhou University, Changzhou 213164, PR China
[c] Department of Mechanical & Construction Engineering, Faculty of Engineering and Environment, Northumbria University, Newcastle upon Tyne, NE1 8ST, UK
[d] Hubei Key Laboratory of Resources and Ecological Environment Geology, Wuhan 430034, PR China
[e] Huzhou Electric Power Design Institute Co., Ltd, Huzhou City, 313000 Zhejiang, PR China

ARTICLE INFO

Keywords:
AuPt nanoparticle
Catalytic activity
Durability
Oxygen reduction reaction
Al-air battery

ABSTRACT

A series of AuPt nanoparticles supported on multi-walled carbon nanotubes (Au_xPt/MWNTs) catalysts with ultrafine distribution ($d \approx 3.0$ nm) were synthesized for Al-air battery cathode to enhance the oxygen reduction reaction. Among them, $Au_{0.67}Pt$/MWNTs catalyst with metal loading of 10.2 wt% (Au:4.1 wt%, Pt:6.1 wt%) exhibited a superior ORR catalytic activity and competitive durability to 20 wt% Pt/C catalyst. When applied as Al-air battery, appropriate increasing Au loading encourage better battery performance. $Au_{1.68}Pt$/MWNTs with 8.95 wt% of Au and as little as 5.3 wt% Pt content exhibit larger specific capacity (921 mAh g^{-1}) and power density (146.8 mW cm^{-2}) as well as better durability than 20 wt% Pt/C catalyst when it is assembled as cathode in Al-air battery.

1. Introduction

Metal-air batteries, such as Zn-air batteries, Mg-air batteries, Al-air batteries are a class of safe, reliable, and efficient energy storage devices have attracted increasing attention [1]. Research has proven they have much higher theoretical energy density than that of state-of-the-art Li-ion battery by producing electric energy through a redox reaction between metal and oxygen [2,3]. Among them, Al-air batteries possess great potential for large scale application due to the high specific capacity (2.98 Ah g^{-1}) and energy density (8100 Wh kg^{-1}), abundant resources of aluminum, environmentally friendly nature with high recyclability etc [4,5]. However, the sluggish kinetics of oxygen reduction reaction (ORR) normally resulting in serious cathode polarization and low energy efficiency is one of the serious issues hindering the wide commercialization of Al-air batteries [6,7].

Platinum (Pt) nanoparticles (NP) dispersed on active carbon materials (Pt/C) has been commonly used to effectively prompt the ORR process, however, it suffers from high cost, low utilization efficiency and poor durability [8,9]. Tremendous efforts have been devoted on the development of low or non-Pt ORR catalysts [10], and the incorporation of other transition metals was reported to simultaneously enhance the ORR activity and durability [11,12]. It has been reported that transition metal (M) such as, Ag, Pd, Cu, Fe, Ni etc. are introduced to form Pt-M alloy or bimetallic catalysts to reduce Pt loading, increase utilization efficiency, high activity and stability. Among the transition metals, gold (Au) is a special candidate in view of its higher oxidation potential than Pt, which encourage the combination of Au and Pt to be a stable catalyst [13,14].

The alloying of Pt with Au is a direct way of incorporation, which was reported to exert apparent effect on the electronic structure owing to the strong coupling between Pt and Au atoms, resulted in attractive ORR catalytic activity [12,15-17]. The problem is that Pt and Au are not always miscible in a whole range of concentrations and phase segregation can be expected, which influence the stability of catalyst seriously [18]. As an alternative choice, forming core (Au) -shell (Pt) structure has been reported to suppress the degradations of Pt nanoparticles (NPs) by up-shifting the dissolution potential of Pt and thereby pledging good long-term stability [19-24]. Shi et al. prepared Au-Pt core–shell catalyst in size of 30 ~ 75 nm aided by ionic liquid, which effectively improved the ORR catalytic activity and stability in comparison to the Pt/C

* Corresponding authors.
E-mail addresses: terence.liu@northumbria.ac.uk (T.X. Liu), luokun@cczu.edu.cn (K. Luo).

https://doi.org/10.1016/j.apsusc.2021.150474
Received 27 March 2021; Received in revised form 6 June 2021; Accepted 23 June 2021
Available online 27 June 2021

catalyst, because of the high utilization of Pt and the protection of Pt active sites by Au [23]. Further increasing the stability of Au-Pt core–shell can be achieved by doped Au core with titanium oxide at vertex and edges, which restricted to much Au segregation on to the Pt at surface facets, as reported by Hu et al [21].

In a reverse way to fabricate Au-Pt core–shell catalyst, decorating Pt surface with Au atoms to protect the vulnerable sites at edges and corners was also reported [25-27]. Kodama et al. deposited Au atoms on step sites of Pt single-crystal surface, which raised the ORR activity by 70% and also improved the durability of Pt [27]. Moreover, Takahashi et al., modified the edges and corners of Pt nanoparticles with arc-plasma deposition, the stability as well as the activity of Pt catalysts was improved significantly [25,26]. With this physical vapour deposition technique, the deposited amounts and deposition site of Au on Pt catalysts is easy to control.

Recent attempts are addressed to develop bimetallic AuPt nanosize catalysts, which has been proved that Au clusters confer stability by raising the Pt oxidation potential and stabilizing Pt against dissolution under harsh work environment [28,29]. Zheng et al. synthesized smaller AuPt NPs ($d \approx 5$ nm) in form of popcorn-like aggregates clusters (in size of ca. 36 nm), which only exhibited better ORR catalytic activity than 10 wt% Pt/C, poorer than 20 wt% Pt/C possibly due to the aggregated structure [29]. It is known that increase the particles size can improve the stability, but sacrifice the activate surface area therefore the catalytic activity. Further investigation to synthesis AuPt catalysts with low metal loading, high activity and stability still need further investigation.

Following this context, we synthesized a series of Au_xPt/MWNTs catalysts (x = 0.25, 0.67, 1.68 and 4.55 of atom ratio) by a simple one-pot reduction of chloroauric acid and chloroplatinic acid with the tris (hydroxylmethyl)phosphine oxide (THPO) in presence of MWNTs. The synthesized Au_xPt NPs are highly dispersed with an average diameter of ca. 3.0 nm. The $Au_{0.67}Pt$/MWNTs catalyst with metal loading of 10.2 wt % (Au:4.1 wt%, Pt:6.1 wt%) exhibited a competitive ORR catalytic activity and durability to 20 wt% Pt/C catalyst. The $Au_{1.68}Pt$/MWNTs by properly increasing Au loading to 8.95 wt% (Pt:5.3 wt%) as the Al-air battery cathode showed larger capacity and power density, superior durability than 20 wt% Pt/C cathode.

2. Experimental section

2.1. Chemicals and materials

Commercial platinum catalyst (Pt/C, 20 wt% and 10 wt%, Alfa Aesar), chloroauric acid ($HAuCl_4$, 99.999%, Shanghai Titan Scientific Co. Ltd., China), tetrakis(hydroxylmethyl) phosphonium chloride (THPC, 80% aqueous solution, Sigma-Aldrich), Nafion solution (5 wt%, Sigma-Aldrich) and multi-walled carbon nanotubes (MWNTs, diameter = 10 ~ 20 nm, length = 10 ~ 30 mm) were used directly without further treatment. Chloroplatinic acid (H_2PtCl_6, 37%), potassium hydroxide (KOH, AR), sodium hydroxide (NaOH, AR) and hydrogen peroxide (H_2O_2, AR, 30% aqueous solution) are purchased from Sinopharm Chemical Reagent Co., Ltd.

2.2. Synthesis of bimetallic Au_xPt/MWNTs catalysts

The MWNTs was pretreated using a moderate surface oxidation to increase water affinity [13,30]. Typically, 200 mg of MWNTs was added in a gas-proof Erlenmeyer flask with a separating funnel in connection to a vacuum pump. The flask was vacuumed to a pressure of 0.01 MPa for 10 min, then 40 mL of deionized water and H_2O_2 mixture was added. The suspension was then sonicated for 10 min followed mixing for 2 h using magnetic stirrer, then kept still overnight. The pre-treated MWNTs were separated from the suspension by centrifuging at 8000 rpm, then dried in an oven at 80 °C overnight.

43 mg of the treated MWNTs were added into 95 mL of deionized water at 75 °C and mixed using ultrasonic for 5 mins, and then 1 mL of 24.3 mM $HAuCl_4$ and 1.25 mL of 20 mM H_2PtCl_6 were added, followed by addition of 600 μL of 1 M NaOH and 2 mL of 50 mM THPC. It was kept stirring for further 3 h at 75 °C to make uniform suspension, and then transferred to ice bath and stood overnight. The product was rinsed with deionized water till pH neutral, and using a freeze-dryer. the obtained hybrid was named as $Au_{1.68}Pt$/MWNTs. Three other hybrids were synthesized using the same procedure with different volumes content of $HAuCl_4$ and H_2PtCl_6 solution, specifically, with 0.333 mL of $HAuCl_4$ and 2.083 mL of H_2PtCl_6, 0.5 mL of $HAuCl_4$ and 1.875 mL of H_2PtCl_6, 1.5 mL of $HAuCl_4$ and 0.625 mL of H_2PtCl_6, the catalysts are marked as $Au_{0.25}Pt$/MWNTs, $Au_{0.67}Pt$/MWNTs and $Au_{4.55}Pt$/MWNTs, respectively.

2.3. Characterization

Catalyst morphology and elemental analyses were carried out using a spherical aberration corrected field emission transmission electron microscope (TEM, Titan G2 60–300) operated at 200 kV. The structure of the catalysts was characterized by an X-ray diffractometer (XRD, PANalytical) equipped with Cu kα radiation. The chemical component of the catalysts was investigated using an X-ray photoelectron spectroscope (XPS, ESCALAB 250Xi, Thermo Fisher Scientific) using Al kα radiation. The metal loading in the catalysts was examined by an inductively coupled plasma mass spectrometer (ICP-MS, X-Series II, Thermo Fisher Scientific), where the hybrids were calcinated at 400 °C for 2 h and then 500 °C for 5 h in air to burn up the MWNTs substrate, after cooling to 200 °C the residuals were treated with aqua regia. The ICP-MS technique was used to determine the metal content in the solution, where each sample was tested for three times, taking the average value as the loading amount of Au and Pt for each sample.

2.4. Electrochemical performance measurement

4 mg of a Au_xPt/MWNTs catalyst, 100 μL of Nafion solution, 200 μL ethanol and 800 μL deionized water are used to prepare the catalyst ink, the slurry was mixed using an ultrasonic sound bath for 30 mins. Cyclic voltammetry (CV) analysis was performed by using an electrochemical workstation (CHI660E, CH Instruments) at a scan rate of 20 mV s^{-1} in N_2 or O_2 saturated 0.1 M KOH solutions. The working, counter and reference electrodes are glassy carbon electrode (GCE, $d = 4$ mm, $S = 0.126$ cm^2), platinum wire and Ag/AgCl electrode, respectively. 8 μL of the catalyst slurry was dropped on the GCE, it was dried in ambient temperature to obtain a smooth coverage on the electrode with catalyst loading of 0.23 mg cm^{-2}. All potential values were given with the respective to reversible hydrogen electrode (RHE) scale, the potentials were converted from Ag/AgCl electrode by using $\varphi_{testvsRHE} = \varphi_{testvsAg/AgCl} + 0.209 + 0.059pH$,where $\varphi_{testvsRHE}$and $\varphi_{testvsAg/AgCl}$is the testing potential verse RHE and Ag/AgCl reference electrode, respectively, 0.209 is the standard potential of Ag/AgCl electrode. The relationship between $\varphi_{RHE}$and pH are showed in Fig.S1.

The ORR kinetics of the Au_xPt/MWNTs hybrid was examined using linear scan voltammetry (LSV) method. ORR kinetics was investigated using rotating disk electrode (RDE) and rotating ring-disk electrode (RRDE) technologies in O_2 saturated 0.1 M KOH. The rotating speed were 400 rpm, 625 rpm, 900 rpm, 1225 rpm and 1600 rpm with the scan rate at 5 mV s^{-1} for RDE. The RRDE equipped with a glassy carbon disk electrode ($d = 4$ mm, $S = 0.126$ cm^2) and a Pt ring electrode ($S = 0.189$ cm^2) and it was performed at scan rate of 1600 rpm only. In the experiment, the disk potential scanned from 1.0 to 0.2 V at a rate of 5 mV s^{-1}, and the ring potential was fixed at 1.8 V. Prior to testing, 5 μL and 8 μL of the catalyst slurry were coated and dried on the RDE and RRDE with catalyst loading of 0.25 and 0.23 mg cm^{-2}, respectively.

Al-air battery performance were measured in a homemade testing cell fabricated with Al foil anode (99.99%, 4.5 cm^2), 4 M KOH electrolyte and air cathode. The air cathode comprises of a current collector (Ni

foam) and a carbon paper (1 cm^2) coated with 2 mg catalyst layer. The discharge polarization curves were carried out at 1 mV s^{-1} between the potential widow of 1.8–0 V vs. Al. the specific capacity was recorded at 100 mA cm^{-2}, the dynamic galvanostatic measurement were performed between 1 mA cm^{-2} and 200 mA cm^{-2}, the durability of air electrode was tested by discharging five cycles by replacing Al anode and electrolyte after each discharge.

3. Results and discussions

3.1. Physical characterization

As shown in Table 1, the overall Au and Pt loading amounts of the $Au_{4.55}Pt$/MWNTs, $Au_{1.68}Pt$/MWNTs, $Au_{0.67}Pt$/MWNTs and $Au_{0.25}Pt$/MWNTs catalysts are measured as 15.05 wt%, 14.25 wt%, 10.2 wt% and 9.5 wt% by the ICP-MS analysis, from which the exact Au/Pt ratios of the catalyst are determined as 4.55, 1.68, 0.67 and 0.25, respectively.

Fig. 1 a1, b1 and c1 illustrate the TEM images of $Au_{4.55}Pt$/MWNTs, $Au_{1.68}Pt$/MWNTs and $Au_{0.67}Pt$/MWNTs catalysts, respectively, along with the corresponding ones in higher magnification shown in Fig.1 a2, b2 and c2. All Au_xPt NPs are deposited uniformly on the MWNTs substrates. The average particle size of the $Au_{4.55}Pt$ on MWNTs is measured in the picture as 3.02 nm, the $Au_{1.68}Pt$ as 2.98 nm, and the $Au_{0.67}Pt$/MWNTs as 2.96 nm, suggesting that the variation of Au/Pt ratios did not influence much on the size of the bimetallic Au_xPt NPs. In the high-resolution TEM (HRTEM) images in Fig. 1 a3, b3 and c3, two *d*-spacing values of 0.236 nm and 0.225 nm are measured, assigned to the Au (1 1 1) and Pt (1 1 1) facets, respectively [31]. The high-angle annular dark field scanning transmission electron microscopy (HAADF-STEM) images in the Fig. 1 a4, b4 and c4 display that the Au and Pt NPs stay overlapped but do not grow together. The energy dispersive X-ray (EDX) analyses in Fig. 1 a5, b5 and c5 also display that Au (green color) and Pt (red color) NPs are very close to each other, implying the possible interaction between the Au and Pt NPs.

XRD patterns of three Au_xPt/MWNTs catalysts in Fig. 2 present the same feature. The peak at 26.6° can be assigned to the (0 0 2) facet of MWNTs (JCPDF No. 25–0284), and the peaks at 38.1°, 44.3°, 64.5° and 77.5° are corresponding to (1 1 1), (2 0 0), (2 2 0) and (3 1 1) facets of Au (JCPDF No. 04–0784). The peaks at 39.5°, 45.9°, 67.0° are attributed to (1 1 1), (2 0 0) and (2 2 0) facets of Pt (JCPDF No. 87–0636), where the diffractions of Pt are enhanced with the decrease of the Au/Pt ratio. No signal assigned to AuPt alloy is seen in the XRD patterns.

Fig. 3 displays the XPS analysis results for Au_xPt/MWNTs catalysts. The high-resolution signals of C_{1s} for the three hybrids (column *a*) are fitted with three peaks at 284.8 eV, 285.2 eV and 286 eV in correspondence to C-H/C-H, C-P-O and C-OH groups, respectively[32]. The P_{2p} signals (column *b*) present two fitting peaks at 133.8 eV and 134.7 eV in each curve, assigned to $P_{2p3/2}$ and $P_{2p1/2}$ groups [32]. The resolved Au_{4f} signals (column *c*) manifest a doublet at 84.3 eV and 87.9 eV, attributed to the $4f_{7/2}$ and $4f_{5/2}$ of metallic Au [13]. The Pt_{4f} signal (column *d*) can be fitted into a doublet at 71.4 eV and 74.7 eV associated with metallic Pt, and the peaks at 72.5 eV and 75.8 eV are attributed to the divalent state of Pt (Pt^{2+}) [23,24]. The results indicate of triphenylphosphine oxide (THPO) as the capping molecule on the Au_xPt NPs, which is normally generated from the cleavage of THPC in alkaline solutions [30].

Table 1
ICP-MS analysis of the Au_xPt/MWNTs catalysts.

Hybrid	Loading amount (wt.%)			Atomic ratio
	Total	Au	Pt	Au : Pt
$Au_{4.55}Pt$/MWNTs	15.05	12.35	2.7	4.55
$Au_{1.68}Pt$/MWNTs	14.25	8.95	5.3	1.68
$Au_{0.67}Pt$/MWNTs	10.2	4.1	6.1	0.67
$Au_{0.25}Pt$/MWNTs	9.5	1.9	7.6	0.25

3.2. Electrochemical ORR performance

The CV plots of the Au_xPt/MWNTs catalysts and 20 wt% Pt/C catalyst are recorded in both O_2 and N_2 saturated 0.1 M KOH ranging from 1.2 V to 0 V at a scanning rate of 20 mV s^{-1}. In hydrogen underpotential deposition (H_{UPD}) region, peaks observed between 0 V and 0.4 V attributed to hydrogen adsorption and desorption. For the $Au_{4.55}Pt$/MWNTs hybrid, Fig. 4a exhibits an oxygen reduction peak at 0.86 V with the current density of 0.86 mA cm^{-2} in O_2 saturated 0.1 M KOH solution, in contrast to the curve in N_2 saturated electrolyte. With the decrease of the Au/Pt ratio, the reduction peak potential of the $Au_{1.68}Pt$/MWNTs and $Au_{0.67}Pt$/MWNTs catalysts shifts positively to 0.866 V and 0.87 V, respectively, along with larger peak current densities of 0.93 mA cm^{-2} and 0.96 mA cm^{-2}. Further decreasing the Au/Pt ratio, the reduction peak potential of $Au_{0.25}Pt$/MWNTs shift positively to 0.876 V, however, the peak current decays to 0.64 mA cm^{-2} as showed in Fig.S2. In comparison, the 20 wt% Pt/C catalyst exhibits an oxygen reduction peak at 0.886 V with the current density of 0.44 mA cm^{-2}. The CV plots of MWNTs were also measured (see Fig.S3), which presented a reduction peak at 0.736 V with the current density of 0.241 mA cm^{-2} in O_2 saturated 0.1 M KOH solution, demonstrating that MWNTs has weak catalytic activity towards oxygen reduction reaction, decorating with AuPt NPs improve the ORR activity significantly. It is seen that all the Au_xPt/MWNTs catalysts present larger reaction current densities than the 20 wt% Pt/C catalyst for oxygen reduction.

The RDE experiment was also used to characterize the ORR performance of the Au_xPt/MWNTs catalysts in O_2-saturated 0.1 M KOH solutions. The onset potential (E_{onset}) and half-wave potential ($E_{1/2}$) are used to characterize the ORR catalytic activity, defined as the potentials at 5% and 50% of the diffusion-limited current density, respectively. The RDE polarization curves of the Au_xPt/MWNTs catalysts, MWNTs and commercial Pt/C can be found in Fig. 5a and Fig.S4 and Fig.S5. Compare to MWNTs, the diffusion-limited current density of Au_xPt/MWNTs increase significantly. It is found that with Au/Pt ratio changes from 4.55 to 1.68 and 0.67, the diffusion-limited current density increases, it then decays when the Au/Pt ratio further decrease to 0.25, thus the $Au_{1.68}Pt$/MWNTs and $Au_{0.67}Pt$/MWNTs exhibits the largest diffusion-limited current density. The loading mass of Pt for all Au_xPt/MWNTs is less than 10 wt%, but the diffusion-limited current density is larger than that of 10 wt% Pt/C.

The mechanism of ORR process can be studied by using the Koutecky-Levich (K-L) plots (Fig. 5b and Fig.S4 and S5), with indication of the relationship between the inverse square root of the rotating rate ($\omega^{-1/2}$) and the reciprocal of current density (J^{-1}), and the following equations are used to calculated the overall electron transfer number (*n*):

$$J^{-1} = J_k^{-1} + J_L^{-1} = J_k^{-1} + (B\omega^{1/2})^{-1} \quad (1)$$

$$B = 0.2nFC_{O_2}(D_{O_2})^{2/3}\upsilon^{-1/6} \quad (2)$$

where J_k is the kinetic current density, J_L is the diffusion-limited current density, ω is the angular velocity (rpm), B^{-1} is the slope of K-L plot, *F* is the Faraday constant, C_{O2} (1.2×10^{-6} mol cm^{-3}) and D_{O2} (1.9×10^{-6} cm s^{-1}) are the bulk concentration and diffusion coefficient of dissolved oxygen, and ν (0.01 cm^2 s^{-1}) is the viscosity coefficient. The *n* values are determined from the K-L plots as 3.9 ~ 4.1 for the $Au_{4.55}Pt$/MWNTs (Fig.S4b), 3.8 ~ 4.0 for the $Au_{1.68}Pt$/MWNTs(Fig. 5b), 3.9 ~ 4.1 for the $Au_{0.67}Pt$/MWNTs (Fig.S4d), 3.8 ~ 4.1 for the $Au_{0.25}Pt$/MWNTs (Fig.S4f), 3.6 ~ 3.9 for the 10 wt% Pt/C (Fig.S5b) and 4.1 ~ 4.3 for the 20 wt% Pt/C (Fig.S5d), demonstrating the four-electron pathway towards ORR in alkaline medium. However, the *n* value for the MWNTs is determined as 1.6 ~ 1.9 (Fig.S4h), suggesting a two-electron ORR process in connection with the generation of H_2O_2. Hence, the MWNTs substrate can catalyze oxygen reduction in alkaline medium but show little effect on the ORR performance of the Au_xPt/MWNTs catalysts.

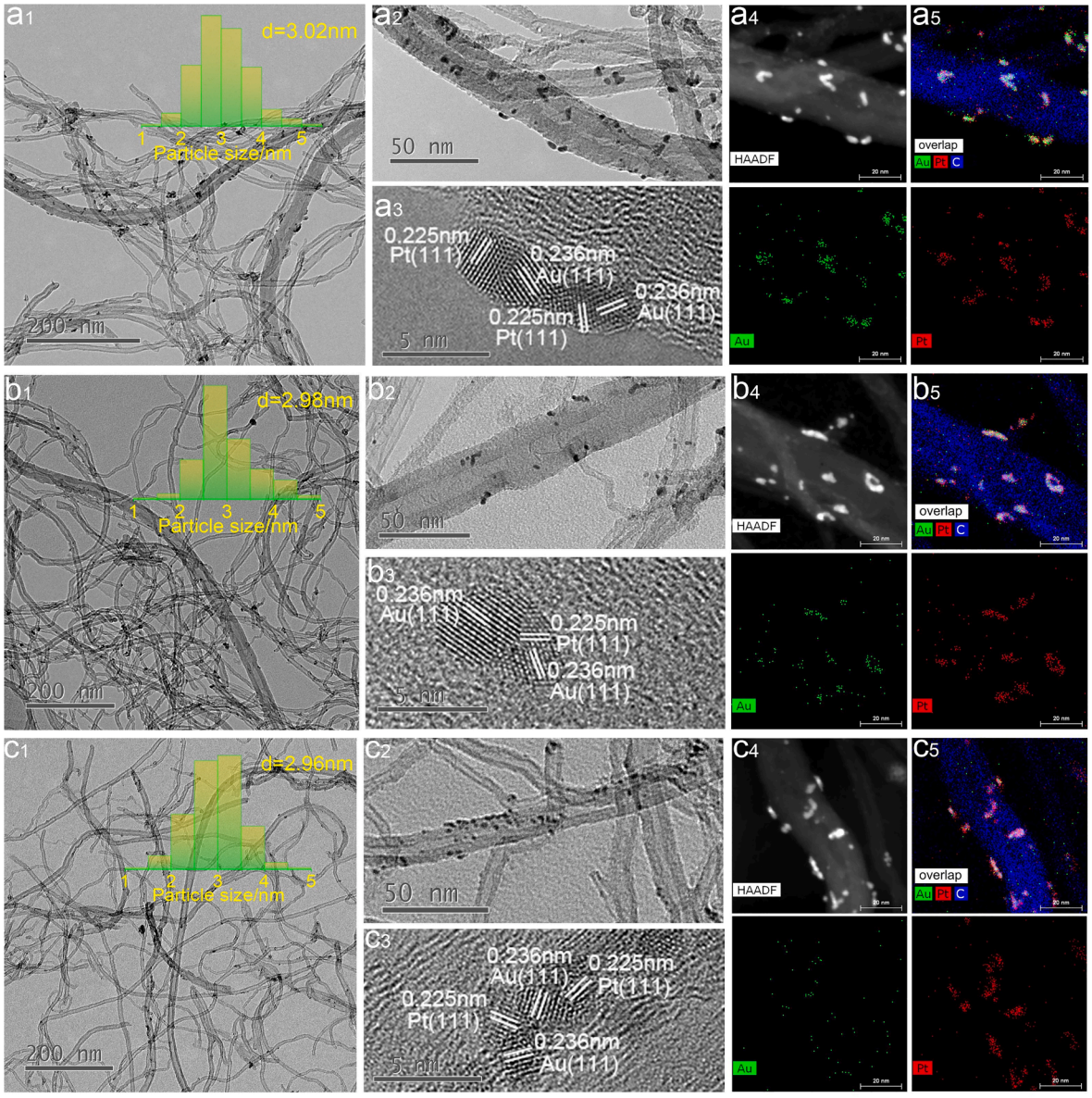

Fig. 1. TEM (a1, b1, c1), zoom-in TEM (a2, b2, c2), HRTEM (a3, b3, c3), HAADF-STEM (a4, b4, c4) and elemental mapping (a5, b5, c5) images of the $Au_{4.55}Pt$/MWNTs(a), $Au_{1.68}Pt$/MWNTs(b) and $Au_{0.67}Pt$/MWNTs (c). Insets: corresponding size distribution plots.

The RDE polarization curves at 1600 rpm of the Au_xPt/MWNTs catalysts are further studied. As displayed in Fig. 5c, the E_{onset} and $E_{1/2}$ values are measured as 1.158 V and 0.890 V for the $Au_{4.55}Pt$/MWNTs, 1.159 V and 0.892 V for the $Au_{1.68}Pt$/MWNTs, 1.150 V and 0.894 V for the $Au_{0.67}Pt$/MWNTs, 1.159 V and 0.895 V for $Au_{0.25}Pt$/MWNTs, 1.151 V and 0.895 V for the 20 wt% Pt/C catalyst, respectively. Compared with the 20 wt% Pt/C, the $Au_{0.67}Pt$/MWNTs and $Au_{1.68}Pt$/MWNTs catalysts manifest comparable values of $E_{1/2}$ and diffusion-limited current. Tafel plots converted from polarization curves shown in Fig. 5d are also used to analyze the ORR kinetics, where the slopes for the $Au_{4.55}Pt$/MWNTs, $Au_{1.68}Pt$/MWNTs, $Au_{0.67}Pt$/MWNTs and $Au_{0.25}Pt$/MWNTs catalysts are determined as 77 mV dec^{-1}, 74 mV dec^{-1} , 72 mV dec^{-1} and 94 mV dec^{-1}, the one for the 20 wt% Pt/C catalyst is 73 mV dec^{-1}, demonstrating that the ORR kinetic of $Au_{4.55}Pt$/MWNTs, $Au_{1.68}Pt$/MWNTs, $Au_{0.67}Pt$/MWNTs is similar to the one of 20 wt% Pt/C catalyst.

Notably, Au_xPt/MWNTs catalysts show significant advantages when compared with the Pt/C catalyst in view of specific activity and mass activity. The electrochemical active surface areas (ECSA) of Pt was measured according to a method reported by Shao-Horn and co-workers [33,34](See ref. Fig. S6), the resulting ECSA of Pt for $Au_{4.55}Pt$/MWNTs, $Au_{1.68}Pt$/MWNTs, $Au_{0.67}Pt$/MWNTs, $Au_{0.25}Pt$/MWNTs and 20 wt% Pt/C is 184.5 m^2 g^{-1}_{Pt}, 204.8 m^2 g^{-1}_{Pt}, 87.9 m^2 g^{-1}_{Pt}, 33.8 m^2 g^{-1}_{Pt}, 90.9 m^2 g^{-1}_{Pt}, and the values of specific activity based on Pt are determined as 0.16 mA cm^{-2}, 0.08 mA cm^{-2}, 0.174 mA cm^{-2}, 0.128 mA cm^{-2}, 0.054 mA cm^{-2} at 0.9 V(Fig. 5e), respectively. The mass loading of Pt was measured using an ICP-MS, results in Table 1, show the Pt contents are 2.7 wt%, 5.3 wt%, 6.1 wt% and 7.6 wt% for $Au_{4.55}Pt$/MWNTs, $Au_{1.68}Pt$/MWNTs, $Au_{0.67}Pt$/MWNTs, $Au_{0.25}Pt$/MWNTs, respectively. The Pt mass activity values are 295 mA mg^{-1}, 164 mA $mg^{-1}$and 153 mA mg^{-1} and 112 mA mg^{-1} for $Au_{4.55}Pt$/MWNTs, $Au_{1.68}Pt$/MWNTs, $Au_{0.67}Pt$/MWNTs and $Au_{0.25}Pt$/MWNTs, which are generally two to six times higher than that of 20 wt% Pt/C (50 mA mg^{-1}) as displayed in Fig. 5f. the metal mass activity while both Au and Pt included are 55 mA mg^{-1}, 61 mA mg^{-1}, 91 mA mg^{-1}, and 89 mA mg^{-1} for $Au_{4.55}Pt$/MWNTs, $Au_{1.68}Pt$/MWNTs, $Au_{0.67}Pt$/MWNTs and $Au_{0.25}Pt$/MWNTs, respectively, higher than the value for the 20 wt% Pt/C catalyst (50 mA mg^{-1}), indicating that the ORR activity increased by decorating Pt with Au cluster. possibly because the interaction between Pt and Au.

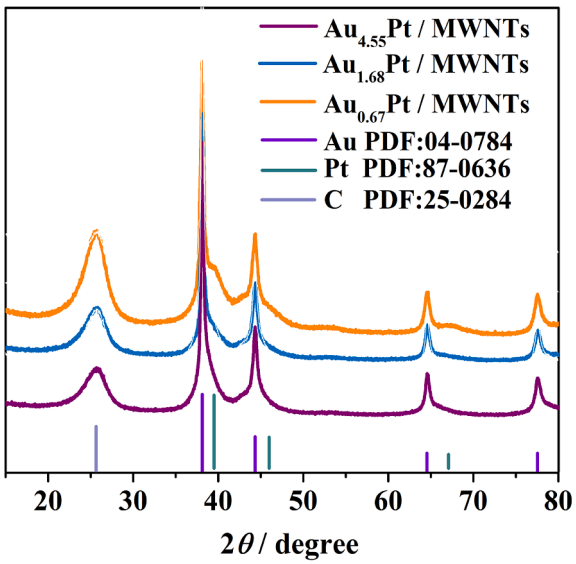

Fig. 2. XRD patterns of $Au_{4.55}Pt$ /MWNTs, $Au_{1.68}Pt$ /MWNTs and $Au_{0.67}Pt$ /MWNTs catalysts.

RRDE measurement was employed to further investigate the oxygen reduction mechanism of the Au_xPt/MWNTs catalysts in 0.1 M KOH. O_2 is reduced on the glassy carbon disk electrode, and the ORR intermediate H_2O_2 is oxidized on the Pt ring electrode. The following equations are used to calculated the overall electron transfer number (n) and the corresponding H_2O_2:

$$n = \frac{4 \times I_d}{I_d + I_r/N} \tag{3}$$

$$H_2O_2\% = 200 \times \frac{I_r/N}{I_d + I_r/N}\% \tag{4}$$

where I_d represents the disk current (A), I_r is the ring current (A), N (collection efficiency) is taken as 44% according to our previous literature [13,30]. Fig. 6a, 6c and 6e illustrate the disk currents of the Au_xPt/MWNTs catalysts increase with the potential scan of disk electrode in the range from 1.2 V to 0.2 V, but the ring current approaches to zero for the Au_xPt/MWNTs catalysts. Fig. 6b, 6d and 6f further illustrate that the H_2O_2 yields are close to zero and the total electron transfer numbers are determined as about 4 for all Au_xPt/MWNTs catalysts, similar as 20wt.% Pt/C (Fig. S8), which again identifies the little contribution of the MWNTs substrate to the catalytic performance of the Au_xPt/MWNTs catalysts.

Apart from the ORR performance, the durability and methanol tolerance are also measured, which are carried out by the current versus time (i-t) chonoamperometry. In the durability tests, the potential was fixed at half-wave potential making the oxygen reduction to take place on the catalysts continuously, and the current was recorded. As shown in Fig. 7a, the reaction currents for all catalysts decrease at the initial stage and then reached plateau. After 30000 s, about 84.6%, 87.5% and 87.8% of initial reaction current is observed for $Au_{4.55}Pt$/MWNTs, $Au_{0.67}Pt$/MWNTs and 20 wt% Pt/C, respectively. In contrast, $Au_{1.68}Pt$/MWNTs exhibits higher stability with 91.6% of current retention, suggesting the superiority in practical application.

In order to investigate the methanol tolerance of Au_xPt/MWNTs catalysts, the *I-t* curves at 0.85 V vs RHE in O_2-saturated 0.1 M KOH solution with the addition of 3 M methanol were recorded. As shown in Fig. 7b, apparent current decay is seen for the 20 wt% Pt/C catalyst soon after a current fluctuation in response to the addition of methanol, leaving only 44% of the initial value at 1400 s. In contrast, the current retention values are about 91%, 88% and 80% for the $Au_{4.55}Pt$/MWNTs, $Au_{1.68}Pt$/MWNTs and $Au_{0.67}Pt$/MWNTs catalysts. It is noteworthy that the superior methanol tolerance of Au_xPt/MWNTs catalysts to the Pt/C catalyst associates with the incorporation of Au NPs, in other words, the Au NPs serve to protect the Pt NPs from poisoning to some extent via particular interaction. The superior methanol tolerance of Au_xPt/MWNTs catalyst also endow the application in direct methanol fuel cell.

3.3. Al-air battery performance of Au_xPt/MWNTs catalysts

The Au_xPt/MWNTs catalysts are then investigated as cathode in a home-made cell Al-air cell illustrated in Fig. 8a. The cell consists an Al anode, air cathode and 4 M KOH electrolyte. For comparison propose, the battery performance of 20 wt% Pt/C was also tested. As showed in Fig. 8b, the cell with $Au_{4.55}Pt$/MWNTs presents the lowest open circuit potential (OCP), which starts at 1.69 V but decays quickly to 1.43 V in half an hour followed by further gradual decrease to 1.36 V during 5 h. The OCP of the cell with $Au_{1.68}Pt$/MWNTs starts at 1.78 V, then declines

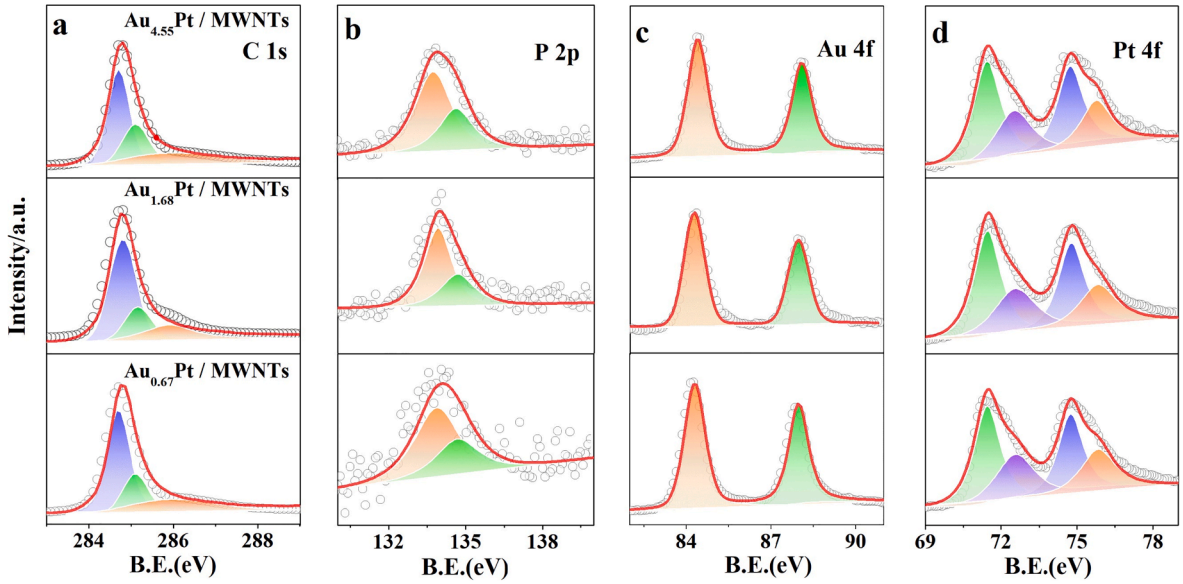

Fig. 3. XPS spectra and fittings for the $Au_{4.55}Pt$/MWNTs (top), $Au_{1.68}Pt$ /MWNTs (middle) and $Au_{0.67}Pt$ /MWNTs (bottom) catalysts: a- C_{1s} spectra; b- P_{2p} spectra; c- Au_{4f} spectra; d- Pt_{4f} spectra.

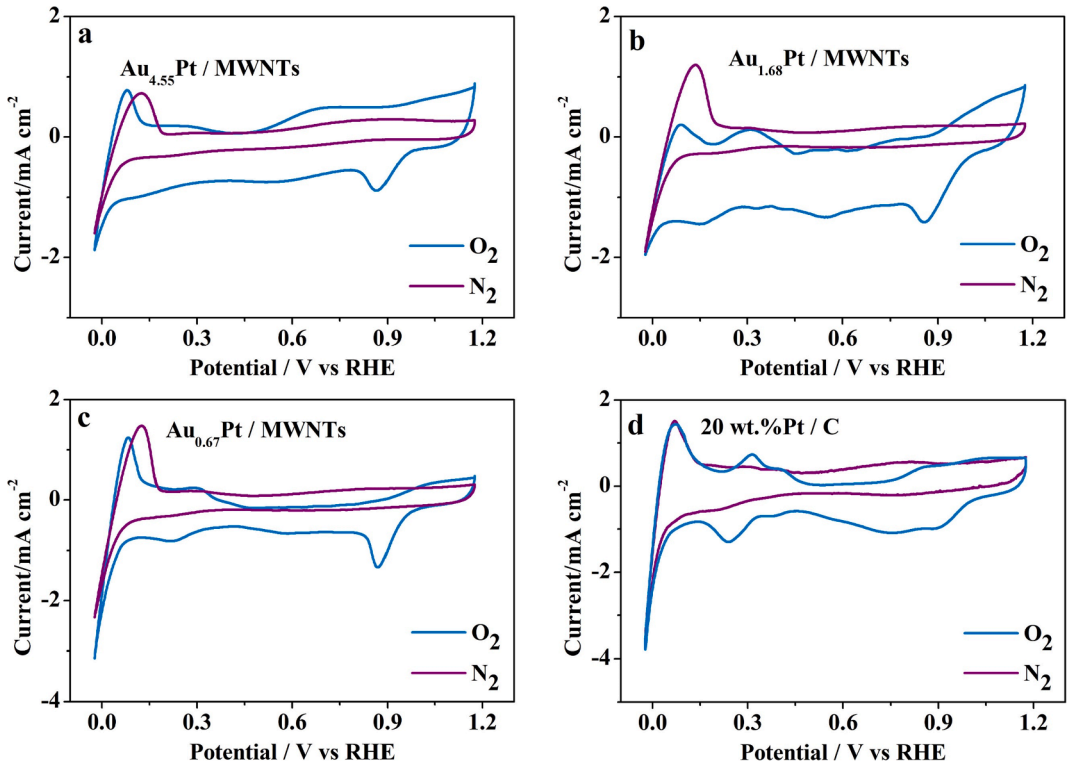

Fig. 4. CV plots of the $Au_{4.55}Pt$/MWNTs (a), $Au_{1.68}Pt$ /MWNTs (b), $Au_{0.67}Pt$/MWNTs (c) and 20 wt% Pt/C catalyst (d) in N_2 and O_2 saturated 0.1 M KOH solutions.

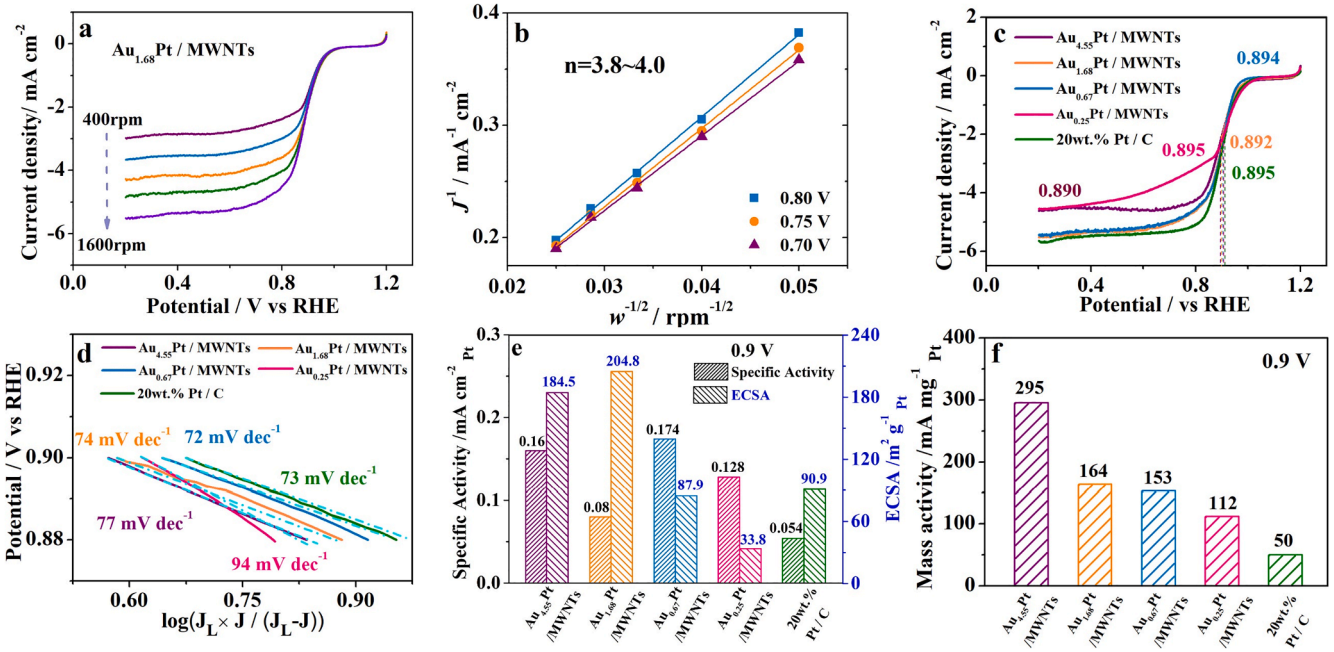

Fig. 5. RDE polarization curves at different rotating rates (a) and corresponding K-L plots (b) of $Au_{0.67}Pt$ /MWNTs, RDE polarization curves at 1600 rpm (c), Tafel plots (d), specific activity (e) and mass activity (f) Pt mass activity for the $Au_{4.55}Pt$/MWNTs, $Au_{1.68}Pt$/MWNTs, $Au_{0.67}Pt$ /MWNTs, $Au_{0.25}Pt$/MWNTs and the 20 wt% Pt/C catalyst.

slightly to 1.67 V and maintained stable till the end of the testing. The cell with $Au_{0.67}Pt$/MWNTs also has a starting OCP of 1.78 V, it declines to 1.55 V slowly during the 5 h testing. Although the OCP of the battery with 20 wt% Pt/C starts at 1.88 V, it decreases to below 1.63 V after 5 h. Fig. 8c exhibits the discharge behavior of Al-air batteries at the current density of 100 mA cm^{-2}. The battery with $Au_{4.55}Pt$/MWNTs has a discharge capacity as large as 939 mAh g^{-1}, however, exhibits the discharge potential lower than 0.8 V. The other three batteries present the discharge potential above 0.9 V, the discharge capacity is 921, 898 and 886 mAh g^{-1} for $Au_{1.68}Pt$/MWNTs, $Au_{0.67}Pt$/MWNTs and 20 wt% Pt/C, respectively. In order to further investigate the performance of hybrid catalysts, the discharge polarization curves and the corresponding powder density curves are recorded as shown in Fig. 8d. The potential decrease sharply for the battery with $Au_{4.55}Pt$/MWNTs, resulting

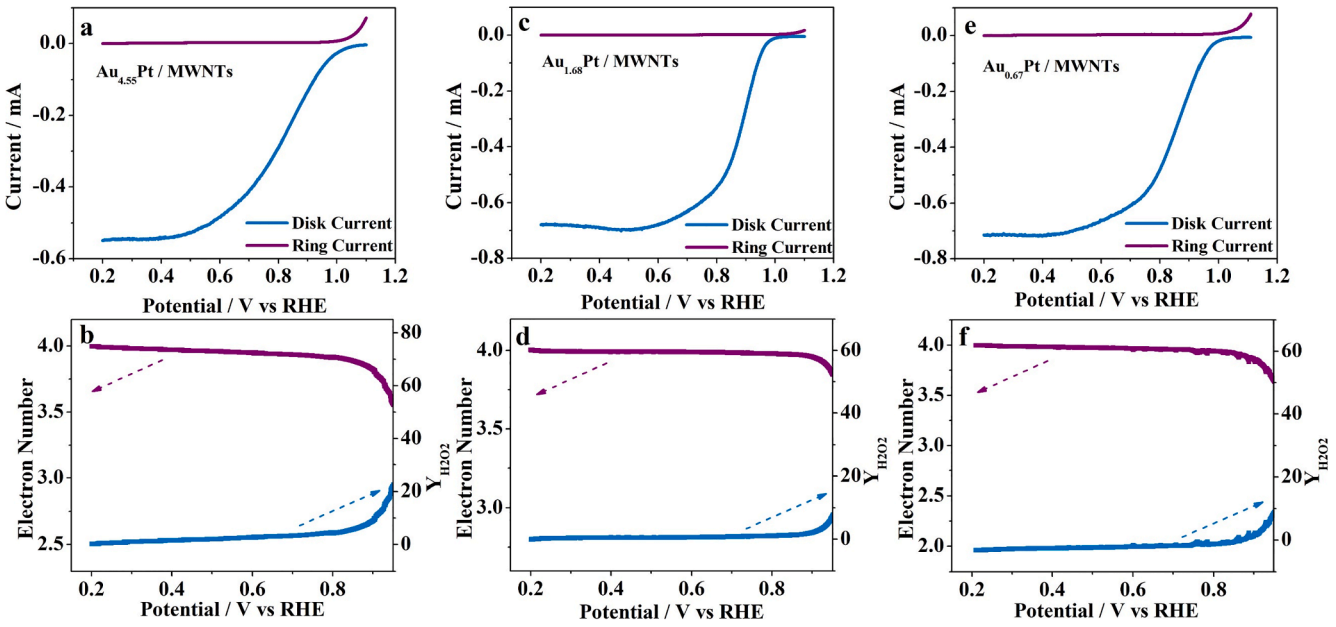

Fig. 6. RRDE polarization curves (a, c, e) and the overall electron transfer number and H_2O_2 yield (b, d, f) of the $Au_{4.55}Pt$ /MWNTs (left column), $Au_{1.68}Pt$ /MWNTs (middle column), $Au_{0.67}Pt$ /MWNTs (right column) catalysts.

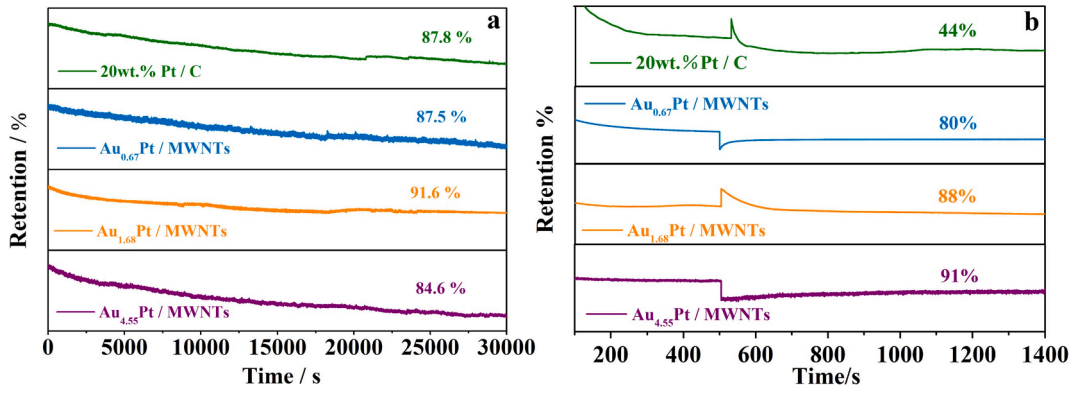

Fig. 7. ORR chronoamperometric response (a) and current–time (i-t) chronoamperometric response by adding of 3 M methanol (b).

in a maximum power density (P_{max}) of 72.7 mW cm^{-2}. In contrast, the potential of the batteries with $Au_{1.68}Pt$/MWNTs, $Au_{0.67}Pt$/MWNTs and 20 wt% Pt/C cathodes decrease much slower, with the corresponding P_{max} of 146.8 mW cm^{-2}, 143.1 mW cm^{-2} and 144.2 mW cm^{-2}, respectively. The assembled Al-air battery with as $Au_{1.68}Pt$/MWNTs cathode can drive a fun working for at least 6 h, (Fig. S9a), and also can drive fan and hygrometer in series running for at least 3 h due to the high powder density (Fig. S9b).

Apart from the above performance, the durability of catalysts is another critical factor to determine the service life of Al-air batteries. Fig. 8e displays the dynamic galvanostatic measurements of the Al-air batteries with $Au_{1.68}Pt$/MWNTs, $Au_{0.67}Pt$/MWNTs and 20 wt% Pt/C cathode, which are tested at the constant current density between 1 and 200 mA cm^{-2}(60 min for each discharge plateau), accordingly, the discharge potential plateau decreases with increasing current density. There is no potential drops observed at each potential plateau with $Au_{1.68}Pt$/MWNTs as cathode. In contrast, with $Au_{0.67}Pt$/MWNTs and 20 wt% Pt/C cathode have potential drop happened often especially at higher current densities. To investigate the long-term stability of the catalysts, potential variations of Al-air batteries are recorded for five cycles which is operated by replacing the Al foil and electrolyte at the end of each cycle, the cathode is reused during these cycles. The potential of all cathodes is dropping at the initial stage and then the discharge plateau occurs. It is obvious that the discharge potential with $Au_{1.68}Pt$/MWNTs cathode is stable for the five cycles, but it drops at the fourth cycle for the ones with $Au_{0.67}Pt$/MWNTs and 20 wt% Pt/C cathode. In order to study the stability of $Au_{1.68}Pt$/MWNTs after long-term operation, the morphology was characterized using TEM and HAADF as showed in Fig.S10. TEM image shows that the nanoparticles aggregated slightly, the HAADF and elemental mapping reveal that Au and Pt nanoparticles are still existed in the formation of bimetal particles, which endows the high stability of $Au_{1.68}Pt$/MWNTs. These above results demonstrate that compared with 20 wt.%Pt/C, the Au_xPt/MWNTs catalysts combines the advantages of high catalytic activity, superior durability, and low cost.

4. Conclusion

Au_xPt/MWNTs catalysts were synthesized by a facile one-pot method, where the ultrafine Au_xPt NPs capped with THPO were uniformly deposited on the MWNTs substrate in an average size of ~ 3.0 nm. The Au_xPt/MWNTs catalysts perform four-electron pathway towards ORR, and exhibit superior catalytic activity in terms of specific activity and mass activity. Amount which, the $Au_{1.68}Pt$/MWNTs catalyst

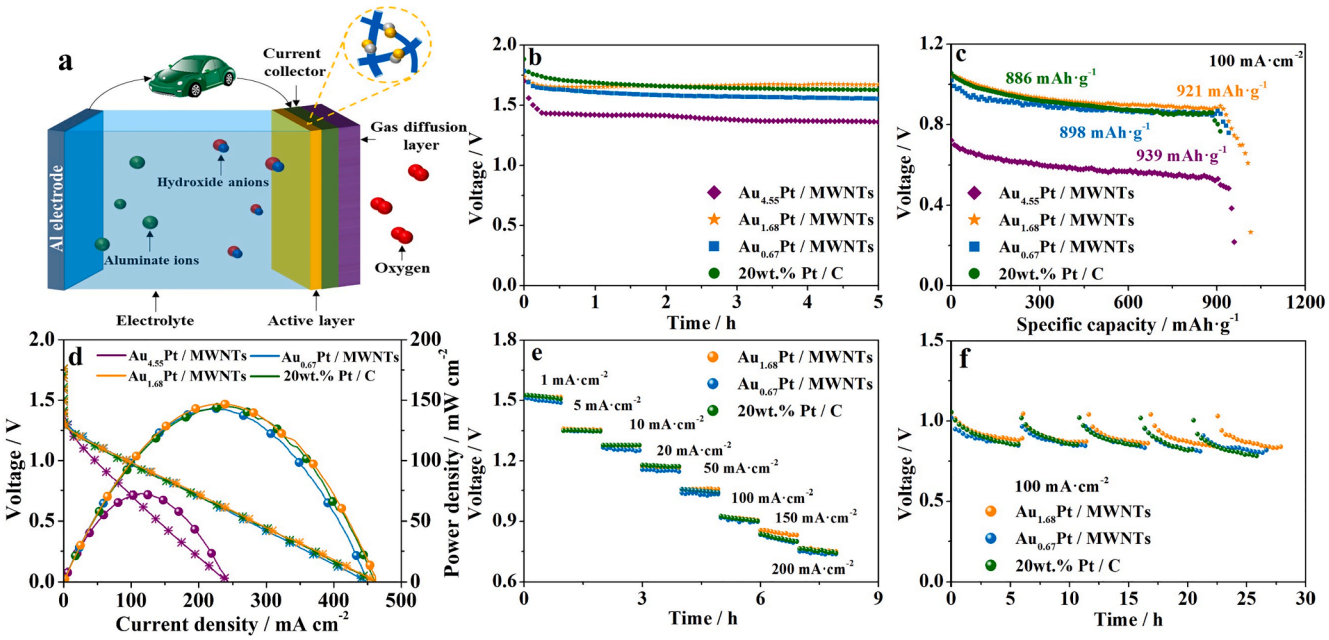

Fig. 8. Al-air battery performance with $Au_{4.55}Pt$/MWNTs, $Au_{1.68}Pt$/MWNTs, $Au_{0.67}Pt$ /MWNTs and 20 wt% Pt/C as cathodes. Schematic illustration of the Al-air battery (a), open circuit plots (b), specific capacities of the Al-air battery (c), discharging polarization curves and corresponding powder density plots (d), dynamic potentiometric measurement from 1 mA cm^{-2} to 200 mA cm^{-2} (e), long-term discharge curves at 100 mA cm^{-2} by replacing Al anode and electrolyte after running out of Al anode.

exhibits higher powder density, higher specific capacity and better durability than 20 wt% Pt/C when used as Al-air cathode. The above results demonstrate the incorporation of Pt and Au NPs enhanced the catalytic performance towards ORR. The excellent catalytic performance and stability of the bimetallic Au_xPt/MWNTs catalysts allow prospective applications as efficient and stable catalysts on Al-air battery and fuel cells at lower Pt usage.

Declaration of Competing Interest

The authors declare that they have no known competing financial interests or personal relationships that could have appeared to influence the work reported in this paper.

Acknowledgement

The work was supported by the National Natural Science Foundation of China (No. 51874051), Guangxi Natural Science Foundation (No. 2018GXNSFAA281184, 2019GXNSFAA245046), Guangxi Key Laboratory of Optical and Electronic Materials and Devices (No. 20KF-4, 20AA-18) and Bagui Scholar Program of Guangxi Province. The authors are also grateful for the assistance from Mr. Xiaobin Zhou from Shiyanjia Lab (www.shiyanjia.com) on materials characterizations.

Appendix A. Supplementary material

Supplementary data to this article can be found online at https://doi.org/10.1016/j.apsusc.2021.150474.

References:

[1] Y. Liu, Q. sun, W. Li, K. Adair, J. Li, X. Sun, A comprehensive review on recent progress in aluminum-air batteries, Green, Energy & Environment 2 (2017) 246–277.
[2] F. Cheng, J. Chen, Metal–air batteries: from oxygen reduction electrochemistry to cathode catalysts, Chemical Society Reviews 41 (2012) 2172–2192.
[3] J. Sun, N. Guo, Z. Shao, K. Huang, Y. Li, F. He, Q. Wang, A facile strategy to construct amorphous spinel-based electrocatalysts with massive oxygen vacancies using ionic liquid dopant, Advanced Energy Materials 8 (2018), 100980.
[4] S. Wu, S. Hu, Q. Zhang, D. Sun, P. Wu, Y. Tang, H. Wang, Hybrid high-concentration electrolyte significantly strengthens the practicability of alkaline aluminum-air battery, Energy Storage Materials 31 (2020) 1248.
[5] S. Wu, Q. Zhang, J. Ma, D. Sun, Y. Tang, H. Wang, Interfacial design of Al electrode for efficient aluminum-air batteries: issues and advances, Materials Today Energy 18 (2020), 100499.
[6] D. Liu, J. Tian, Y. Tang, J. Li, S. Wu, S. Yi, X. Huang, D. Sun, H. Wang, High-power double-face flow Al-air battery enabled by CeO_2 decorated MnOOH nanorods catalyst, Chemical Engineering Journal 406 (2021), 126772.
[7] Y. Wang, J. Hao, J. Yu, H. Yu, K. Wang, X. Yang, J. Li, W. Li, Hierarchically porous N-doped carbon derived from biomass as oxygen reduction electrocatalyst for high-performance Al–air battery, Journal of Energy Chemistry 45 (2020) 119–125.
[8] V. Mazumder, Y. Lee, S. Sun, Recent development of active nanoparticle catalysts for fuel cell reactions, Advanced Functional Materials 20 (2010) 1224–1231.
[9] N. Guo, H. Xue, A. Bao, Z. Wang, J. Sun, T. Song, X. Ge, W. Zhang, K. Huang, F. He, Q. Wang, Achieve superior electrocatalytic performance by surface copper vacancy defects during electrochemical etching process, Angewandte Chemie Intemation Edition 59 (2020) 13778–13784.
[10] D. Chung, J. Yoo, Y. Sung, Highly Durable and active Pt-based nanoscale design for fuel-cell oxygen-reduction electrocatalysts, Advanced Materials 30 (2018) 1704123.
[11] Y. Cao, Y. Yang, Y. Shan, Z. Huang, One-pot and facile fabrication of hierarchical branched Pt-Cu nanoparticles as excellent electrocatalysts for direct methanol fuel cells, ACS Applied Materials & Interfaces 8 (2016) 5998–6003.
[12] T. Bian, H. Zhang, Y. Jiang, C. Jin, J. Wu, H. Yang, D. Yang, Epitaxial growth of twinned Au−Pt core−shell star-shaped decahedra as highly durable electrocatalysts, Nano Letters 15 (2015) 7808–7815.
[13] L. Xiang, Z. Luo, C. Hu, Z. Bian, J. Lu, Y. Cao, K. Luo, Gold nanoparticle/multi-walled carbon nanotube hybrid as a stable catalyst for the oxygen reduction reaction, ChemElectroChem 5 (2018) 1073–1079.
[14] J. Sun, T. Song, Z. Shao, N. Guo, K. Huang, F. He, Q. Wamg, Interfacial electronic structure modulation of hierarchical Co(OH)F/$CuCo_2S_4$ nanocatalyst for enhanced electrocatalysis and Zn-air batteries performances, ACS Applied Materials & Interfaces 11 (2019) 37531–37540.
[15] Y. Fang, Z. Liu, Mechanism of oxygen electro-reduction on Au-modified Pt: Minimizing O coverage and Pt site exposure toward highly stable and active cathode, The Journal of Physical Chemistry C 115 (2011) 17508–17515.
[16] Y. Liang, S. Lin, C. Liu, S. Chung, T. Chen, J. Wang, K. Wang, The performance and stability of the oxygen reduction reaction on Pt-M (M = Pd, Ag and Au) nanorods: an experimental and computational study, Chemical Communications 51 (2015) 6605–6608.
[17] G. Selvarani, S. Selvaganesh, S. Krishnamurthy, G. Kiruthika, P. Sridhar, S. Pitchumani, A methanol-tolerant carbon-supported Pt-Au alloy cathode catalyst for direct methanol fuel cells and its evaluation by DFT, The Journal of Physical Chemistry C 113 (2009) 7461–7468.
[18] P. Hernández-Fernández, S. Rojas, P. Ocón, G. Fuente, J. Fabián, J. Sanza, M. Pena, F. García- García, P. Terreros, J. Fierro, Influence of the preparation route of bimetallic Pt-Au nanoparticle electrocatalysts for the oxygen reduction reaction, The Journal of Physical Chemistry C 111 (2007) 2913–2923.

[19] Y. Ma, H. Zhang, H. Zhong, T. Xu, H. Jin, X. Geng, High active PtAu/C catalyst with core-shell structure for oxygen reduction reaction, Catalysis Communications 11 (2010) 434–437.
[20] L. Shen, G. Zhang, S. Miao, J. Liu, B. Xu, Core–shell nanostructured Au@Ni_mPt_2 electrocatalysts with enhanced activity and durability for oxygen reduction reaction, ACS Catalysis 6 (2016) 1680–1690.
[21] J. Hu, L. Wu, K. Kuttiyiel, K. Goodma, C. Zhang, Y. Zhu, M. Vukmirovic, M. White, K. Sasaki, R. Adzic, Increasing stability and activity of core-shell catalysts by preferential segregation of oxide on edges and vertexes: Oxygen reduction on Ti-Au@Pt/C, Journal of the American Chemical Society 138 (2016) 9294–9300.
[22] L. Zhan, S. Yu, J. Zhang, J. Gong, Porous single-crystalline AuPt@Pt bimetallic nanocrystals with high mass electrocatalytic activities, Chemical Science 7 (2016) 3500–3505.
[23] Y. Shi, S. Chen, J. Feng, X. Lin, W. Wang, A. Wang, Dicationic ionic liquid mediated fabrication of Au@Pt nanoparticles supported on reduced graphene oxide with highly catalytic activity for oxygen reduction and hydrogen evolution, Applied Surface Science 441 (2018) 438–447.
[24] F. Ye, H. Liu, W. Hu, J. Zhong, Y. Chen, H. Cao, J. Yang, Heterogeneous Au-Pt nanostructures with enhanced catalytic activity toward oxygen reduction, Dalton Transactions 41 (2012) 2898–2903.
[25] S. Takahashi, H. Chiba, T. Kato, S. Endo, T. Hayashi, N. Todoroki, T. Wadayama, Oxygen reduction reaction activity and structural stability of Pt-Au nanoparticles prepared by arc-plasma deposition, Physical Chemistry Chemical Physics 17 (2015) 18638–18644.
[26] S. Takahashi, N. Todoroki, R. Myochi, T. Nagao, N. Taguchi, T. Ioroi, F. Feiten, Y. Wakisaka, K. Asakura, O. Sekizawa, T. Sakata, K. Higashi, T. Uruga, Y. Iwasawa, T. Wadayama, Effective surface termination with Au on PtCo@Pt core-shell nanoparticle: Microstructural investigations and oxygen reduction reaction properties, Journal of Electroanalytical Chemistry 842 (2019) 1–7.
[27] K. Kodama, R. Jinnouchi, N. Takahashi, H. Murata, Y. Morimoto, Activities and stabilities of Au-modified stepped-Pt single-crystal electrodes as model cathode catalysts in polymer electrolyte fuel cells, Journal of the American Chemical Society 138 (2016) 4194–4200.
[28] M. Beltrán-Gastéum, M. Salazar-Gastélum, J. Flores-Hernández, G. Botte, S. Perez-Sicairos, T. Romero-Castañon, E. Reynoso-Soto, R. Félix-Navarro, Pt-Au nanoparticles on graphene for oxygen reduction reaction: Stability and performance on proton exchange membrane fuel cell, Energy 181 (2019) 1225–1234.
[29] J. Zheng, S. Li, X. Ma, F. Chen, A. Wang, J. Chen, J. Feng, Popcorn-like PtAu nanoparticles supported on reduced graphene oxide: Facile synthesis and catalytic applications, Journal of Materials Chemistry A 2 (2014) 8386–8395.
[30] L. Guo, L. Xiang, F. Li, X. Liu, L. Xing, D. Li, Z. Luo, K. Luo, Silver nanoparticle/multiwalled carbon nanotube hybrid as an efficient electrocatalyst for the oxygen reduction reaction in alkaline medium, ChemElectroChem 6 (2019) 2489–2496.
[31] J. Zhang, K. Sasaki, E. Sutter, R. Adzic, Stabilization of platinum oxygen-reduction electrocatalysts using gold clusters, Science 315 (2007) 220.
[32] K. Luo, Y. Xiang, H. Wang, L. Xiang, Z. Luo, Multiple-sized amphiphilic janus Gold nanoparticles by ligand exchange at toluene/water interface, Journal of Materials Science & Technology 32 (2016) 733–737.
[33] Y. Lu, Z. Xu, H. Gasteiger, S. Chen, K. Hamad-Schifferli, Y. Shao-Horn, Platinum-gold nanoparticles: A highly active bifunctional electrocatalyst for rechargeable lithium-air batteries, Journal of the American Chemical Society 132 (2010) 12170–12171.
[34] Y. Lu, H. Gasteiger, Y. Shao-Horn, Catalytic activity trends of oxygen reduction reaction for nonaqueous Li-air batteries, Journal of the American Chemical Society 133 (2011) 19048–19051.